Materials Advances

ROYAL SOCIETY OF CHEMISTRY

PAPER

View Article Online
View Journal | View Issue



Cite this: *Mater. Adv.*, 2025, **6**, 7090

# Peptide-based biosensors for variant-specific detection of SARS-CoV-2 antibodies†

Amanda E. Sabaine,[a] Ana C. H. Castro-Kochi,[ab] Rodrigo S. N. Mancini,[a] Marcos R. A. Silva,[a] Anderson F. Sepulveda,[a] Jamille R. Oliveira,[c] Cesar Remuzgo,[d] Keity S. Santos,[cd] Vivian L. Oliveira,[d] Leandro T. Kochi,[a] Lauro T. Kubota,[e] Mónica B. Mamián-López[a] and Wendel A. Alves*[a]

The pandemic has highlighted an urgent demand for reliable methods to track immunological responses against SARS-CoV-2, especially in vaccinated populations and recovered patients. In this study, we developed biosensors based on the immunodominant peptide P44 (sequence: TGKIADYNYKLPDDF), located in a mutation hotspot of the Spike protein's receptor-binding domain (RBD), to enable the ultrasensitive and specific detection of antibodies against SARS-CoV-2. Gold nanoparticles (AuNPs, ~30 nm) were synthesized *via* the Turkevich method and functionalized with P44-WT (wild-type) and its mutated forms, P44-T (gamma) and P44-N (beta), using 4-mercaptobenzoic acid (MBA) as a stabilizer. Functionalization was confirmed by UV-vis spectroscopy and dynamic light scattering (DLS), which revealed shifts in the plasmonic band and increases in the hydrodynamic radius. The optical biosensor, based on surface-enhanced Raman spectroscopy (SERS), analyzed convalescent and control sera ($n$ = 104) using partial least squares discriminant analysis (PLS-DA), achieving 100% sensitivity and 76% specificity. Complementary electrochemical impedance spectroscopy (EIS) on glassy carbon electrodes corroborated the peptide–antibody interaction, yielding detection limits of 0.43, 4.85, and 8.04 ng mL$^{-1}$ for P44-WT, P44-T, and P44-N, respectively. The platform demonstrated high specificity in complex serum matrices and was unaffected by nonspecific biofouling. Our findings underscore the importance of peptide selection and optimization in enhancing biosensor performance and demonstrate the adaptability of this methodology for detecting emerging infectious diseases.

Received 14th May 2025,
Accepted 26th August 2025

DOI: 10.1039/d5ma00485c

rsc.li/materials-advances



## Introduction

The COVID-19 pandemic has underscored the critical need for robust tools to monitor immune responses to SARS-CoV-2, particularly in vaccinated and convalescent individuals. While diagnostics rely on direct pathogen detection, serological surveillance provides invaluable insights into population-level immunity and vaccine efficacy.[1–3] However, conventional serological assays—such as ELISA, CLIA, and LFIA—often lack the sensitivity, scalability, or cost-effectiveness required for large-scale immune monitoring.[4–7] Biosensors, especially those employing synthetic peptides as biorecognition elements, offer a promising alternative due to their high specificity, adaptability, and potential for decentralized use.[8–11] Moreover, peptides enable rapid adaptation to emerging variants: modifying a single residue during synthesis is far simpler and faster than producing a new, mutated full-length protein.[12]

Biomimetic biosensors employ short synthetic peptides designed to mimic biological recognition and selectively bind to target molecules such as viral proteins or antibodies.[13] These peptides can be chemically modified with functional groups to enhance immobilization or signal generation.[14,15] Immobilization onto biosensor surfaces is typically achieved *via* covalent bonding or specific adsorption, ensuring structural stability.[11] Upon target interaction, the biosensor generates electrical or optical signals, which are processed to quantify or identify the analyte. Due to the complex and high-dimensional nature of biosensor data, chemometric tools are essential for identifying relevant spectral features and improving analytical performance.[16]

[a] *Center for Natural and Human Sciences, Federal University of ABC, Av. dos Estados, 5001, Santo André, São Paulo 09210-580, Brazil. E-mail: wendel.alves@ufabc.edu.br*
[b] *School of Biomedical Engineering, Einstein Hospital Israelita, Av. Prof. Francisco Morato, 4293, São Paulo, São Paulo 05521-200, Brazil*
[c] *Department of Clinical Medicine, Discipline of Allergy and Clinical Immunology, Faculty of Medicine, University of São Paulo, Av. Dr Arnaldo, 455, São Paulo, São Paulo 01246-903, Brazil*
[d] *Laboratory of Immunology, LIM19, Heart Institute (InCor), Clinical Hospital of the Faculty of Medicine, University of São Paulo (HCFMUSP), Av. Dr Arnaldo, 44, São Paulo, São Paulo 05403-900, Brazil*
[e] *Institute of Chemistry, State University of Campinas, 13084-971 Campinas, SP, Brazil*

† This article is dedicated to the memory of Prof. Lauro Tatsuo Kubota.

Electrochemical techniques and surface-enhanced Raman spectroscopy (SERS) are particularly powerful for biosensing applications among the available transduction strategies. SERS enhances Raman signals by several orders of magnitude *via* specially engineered nanostructured substrates.[17] While offering rapid and accurate results, this method typically requires specialized instrumentation.[18,19] Electrochemical approaches, by contrast, detect biorecognition events through current, voltage, or impedance changes.[20] These systems offer simplicity, low cost, and miniaturization and are ideal for decentralized testing and real-time diagnostics.[21,22]

Recent studies have demonstrated the potential of synthetic peptides as biorecognition elements.[23] Castro *et al.* developed a label-free electrochemical biosensor using AuNPs and a synthetic peptide to replace the Spike protein.[11] The device achieved 3.4-fold higher sensitivity than conventional Spike-based systems and 100% accuracy in distinguishing between COVID-19 and control sera through machine learning models.[11] Mancini *et al.* applied a similar strategy for visceral leishmaniasis detection *via* a SERS-based platform using peptide-functionalized AuNPs, achieving 100% sensitivity and 88.2% specificity through chemometric analysis.[10]

A main challenge in biosensor design is ensuring analytical robustness against mutations in the target structure. Such mutations can alter molecular conformation and binding dynamics, impacting sensitivity and specificity.[24] Notably, SARS-CoV-2 variants of concern—including alpha (B.1.1.7), beta (B.1.351), gamma (P.1), and delta (B.1.617.2)—harbor mutations in critical genomic regions that may impair test performance.[25] For example, Nunez *et al.* reported signal loss in an electrochemical biosensor using mutated Spike proteins, highlighting the diagnostic vulnerability to such changes.[9,12]

This study employed the immunodominant peptide P44 (sequence: TGKIADYNYKLPDDF), corresponding to residues S415–429 of the receptor-binding domain (RBD) of the SARS-CoV-2 Spike protein. P44 was identified by Oliveira *et al.*[26] using a comprehensive RBD peptide microarray as one of the most frequently recognized linear epitopes in sera from COVID-19 convalescent individuals (68% reactivity), with antibody binding levels positively correlating with viral neutralization titers. Located within a region critical for ACE2 interaction and encompassing the mutation hotspot K417, found in variants such as gamma, beta, and omicron, P44 is particularly suited for biosensor development targeting variant-specific immune responses. Here, we investigate the application of P44 and its mutated counterparts, P44-T and P44-N, in constructing and evaluating electrochemical and SERS biosensors. The biosensors were tested with sera from COVID-19 patients and controls, showing high sensitivity and specificity. Notably, the SERS platform achieved 100% sensitivity and 76% specificity, while electrochemical impedance spectroscopy yielded detection limits in the low nanogram range (0.43–8.04 ng $mL^{-1}$). These results demonstrate the adaptability and suitability of peptide-based biosensors for detecting immune responses to SARS-CoV-2 variants.

# Experimental section

## Materials

Sodium citrate dihydrate (W302600, >99%) and gold(III) chloride trihydrate (520918, >99.9%) were purchased from Sigma-Aldrich (St. Louis, USA). Potassium chloride, sodium hydroxide, and citric acid trihydrate were obtained from Labsynth (São Paulo, Brazil). A phosphate buffer was prepared by neutralizing monobasic sodium phosphate monohydrate with dibasic potassium phosphate. 4-Mercaptobenzoic acid (MBA, CAS: 1074-36-8, 90%) was used as the Raman reporter molecule.

The synthetic immunogenic peptide P44-WT, with sequence S415–429 (TGKIADYNYKLPDDF), comprising 15 residues and molecular weight (MW) of 1758.85 g $mol^{-1}$, was used as the wild-type reference. Two mutated analogs were also tested: P44-T (TGTIADYNYKLPDDF, MW = 1731.80 g $mol^{-1}$) and P44-N (TGNIADYNYKLPDDF, MW = 1744.79 g $mol^{-1}$). All peptides were provided by the InCor Institute (São Paulo, Brazil) and used without further modification.

Sera from 71 COVID-19 convalescent patients were selected for biosensor experiments based on RBD positivity (confirmed by ELISA) and prior reactivity to P44WT in microarray chip and ELISA experiments.[26] For SERS analysis, serum samples were diluted 1 : 10 000 in ultrapure water to prevent contamination or nanoparticle aggregation. For electrochemical experiments, a 1 : 500 dilution was used.

Negative control serum samples were provided by the BCRJ Cell Bank (Brazilian Cell Repository) and were collected before the COVID-19 pandemic, ensuring no exposure to SARS-CoV-2. According to Nunez *et al.*,[9] these samples are positive for four endemic human coronaviruses (HCoV-229E, OC43, NL63, and HKU1) and negative for SARS-CoV-2, as demonstrated by ELISA, confirming the specificity of the assays.[8] All procedures were approved by the Ethics Committee of the Federal University of ABC (CAAE: 43139921.2.0000.5594).

## Synthesis of gold nanoparticles

Gold nanoparticles (AuNPs) were synthesized *via* the classical Turkevich method.[14,27–30] Briefly, 23 mg of $HAuCl_4 \cdot 3H_2O$ were dissolved in 95 mL of ultrapure water and brought to a boil under constant stirring. Then, 3.0 mL of preheated 1% (w/v) sodium citrate dihydrate solution (30 mg) was added. The heating was discontinued after the color change from colorless to red, and stirring was maintained for 5–10 minutes. After cooling to room temperature, the colloidal suspension was diluted to a final volume of 100 mL in a volumetric flask.

## Optical biosensors

The SERS technique was employed to construct the optical biosensor (Fig. 1), using a portable i-Raman Plus spectrometer equipped with a 785 nm laser. Spectra were recorded with a 15-second exposure of 300–2000 $cm^{-1}$. A custom-built sample holder was used to standardize measurements and minimize external light interference.

The support was fabricated using a Creality Ender-3 V2 3D printer and black polylactic acid (PLA) filament. The holder

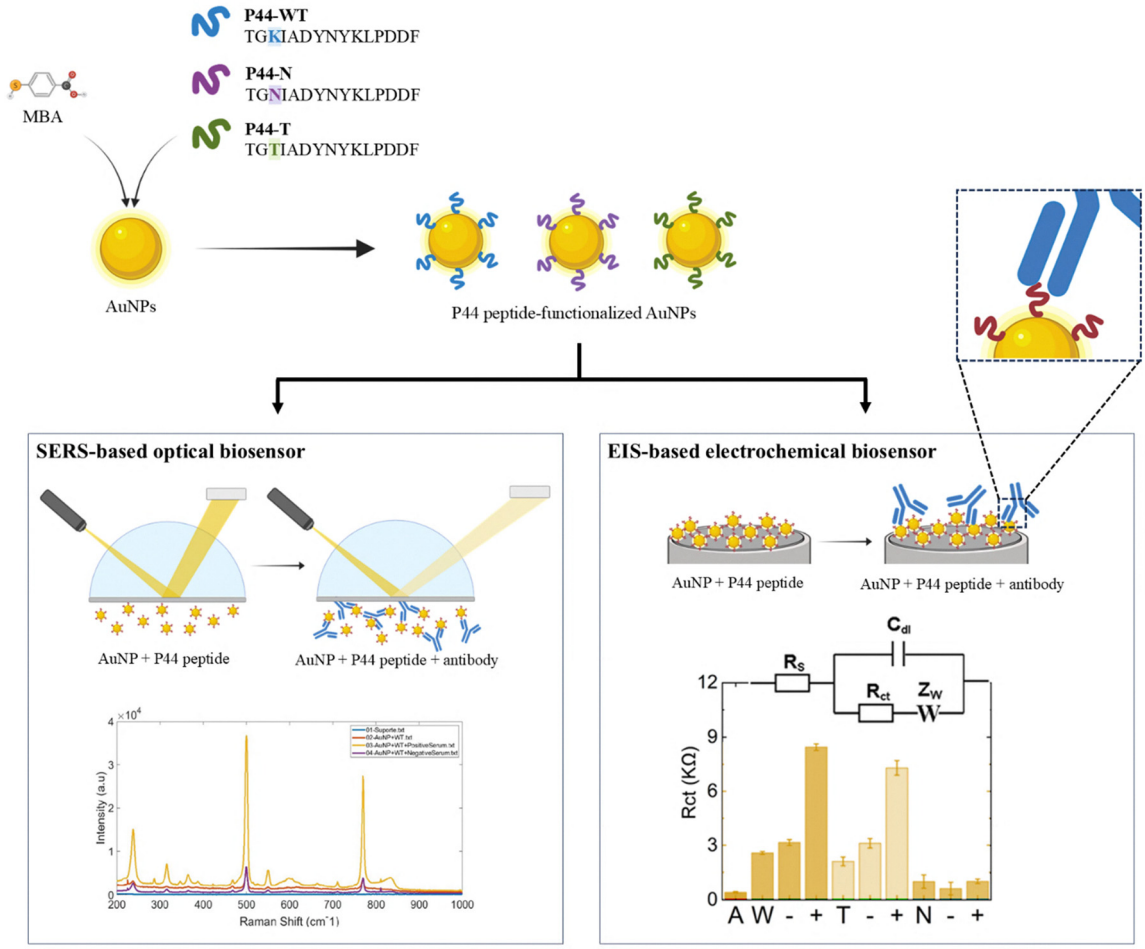


Fig. 1 Schematic representation of the optical and electrochemical biosensor operation. AuNPs were functionalized with the immunodominant P44 peptide in phosphate buffer (pH 6.0) using MBA as a Raman reporter. The biosensor detects antibodies in serum samples from convalescent COVID-19 patients and healthy individuals through Raman-SERS analysis combined with PLS-DA classification and electrochemical impedance measurements.

consisted of two interlocking pieces, each measuring 3.3 × 3.3 cm, with a base height of 0.7 cm and a top height of 0.5 cm. It contained four wells (5.5 mm diameter, 0.5 cm depth), each with a 150 μL capacity, and protective cylindrical extensions designed to house the probe and block ambient light. Wells were spaced 1.0 cm apart (see Fig. S1).

The SERS biosensor was optimized using a central composite rotational design (DCCR). Spectra were preprocessed and integrated, and experimental conditions were modeled using response surface methodology (RSM) with Protimiza and Minitab software.

### Biosensor assembly and measurement protocol

The P44 peptide was immobilized onto citrate-stabilized AuNPs through electrostatic and hydrophobic interactions, following strategies previously reported for peptide–AuNP conjugation.[11] The biosensor was assembled under optimized conditions to functionalize AuNPs with the target peptides (Fig. 1). The final solution consisted of 120 μL of AuNPs, 7 μL of 100 mmol $L^{-1}$ citrate buffer (pH 6.0), 2 μL of P44-WT at 35 mg $L^{-1}$, and 16 μL of MBA, yielding 145 μL of peptide-coated AuNPs (AuNP-P44-WT).

After peptide conjugation, the AuNPs were purified by centrifugation and resuspension steps in ultrapure water to remove unbound peptides and residual reagents. Due to their low molecular weight and lack of sedimentation, unreacted peptides remain in the supernatant after centrifugation, allowing effective isolation of the AuNP–peptide conjugates. The purified conjugates were then redispersed and used immediately in the biosensor assembly.

Blank measurements were obtained by adding 5 μL of ultrapure water to 145 μL of AuNP-P44-WT. Sample measurements were performed by mixing 145 μL of conjugate with 5 μL of the test sample, which consisted of monoclonal antibody, convalescent serum, or negative serum. The same procedure was applied for the mutant peptides P44-T and P44-N, yielding the respective conjugates.

MBA was not used for peptide conjugation, but rather as a Raman reporter molecule in the SERS platform. Its thiol group enables strong adsorption onto the AuNP surface, and its characteristic vibrational bands provide a stable and intense SERS signal. Changes in these spectral features upon antibody binding to the peptide serve as indirect indicators of molecular

recognition at the nanoparticle interface, as previously demonstrated in the literature.[31–34]

### Electrochemical biosensor

To construct the electrochemical biosensor (Fig. 1), a three-electrode system was employed, comprising a glassy carbon (GC) electrode as the working electrode, an Ag/AgCl (3 mol $L^{-1}$ KCl) electrode as the reference, and a platinum wire as the counter electrode. GC electrodes were first mechanically polished using alumina suspensions of decreasing particle sizes on a polishing cloth, followed by ultrasonic cleaning for 15 minutes and rinsing with ultrapure water to ensure surface cleanliness and homogeneity.

The AuNP–peptide conjugate was then deposited onto the GC electrodes by drop-casting 6 μL of the suspension onto the surface. After drying at room temperature, the electrodes were gently rinsed with phosphate buffer (pH 6.0) for 10 seconds under agitation to remove loosely bound material, ensuring reproducible physical adsorption of the conjugates through non-covalent interactions.

Subsequently, the electrodes were incubated for 30 minutes with 6 μL of serum samples from SARS-CoV-2-infected patients diluted 1 : 500 in phosphate buffer. All incubation steps were followed by a 10-second wash with agitation in phosphate buffer at room temperature. After the final rinse, the electrodes were stored under appropriate conditions for subsequent electrochemical analysis.

The buffer solution used throughout the biosensor assays (pH 6.0) had been previously optimized for the P44-WT peptide, providing the highest analytical response in preliminary tests. Although the same condition was applied to P44-T and P44-N to facilitate direct comparison, it may not correspond to their optimal pH for interaction and biorecognition, potentially affecting their performance.

The neutralizing human monoclonal antibody B38 (anti-SARS-CoV-2 RBD) was employed for calibration purposes. Electrochemical measurements were performed in a 0.1 mol $L^{-1}$ KCl solution containing 5 mmol $L^{-1}$ of the $[Fe(CN)_6]^{3-/4-}$ redox couple as the supporting electrolyte. Experiments involving biological components were carried out using ultrapure water.

Although bare AuNPs were not used as electrochemical controls, this decision was based on their lack of specific binding sites for antibody recognition. The biosensing strategy relied on detecting impedance changes resulting from specific interactions between the peptide-functionalized AuNPs and serum antibodies.

All electrochemical analyses were conducted using a Metrohm Autolab PGSTAT 302N system, equipped with an FRA2 electrochemical impedance module, and operated *via* NOVA 2.1.3 software. Electrochemical impedance spectroscopy (EIS) was performed at the half-wave potential ($E_{1/2}$), previously determined by cyclic voltammetry (approximately 240 mV), using a frequency range from 0.1 Hz to 30 kHz.

### Characterization of nanoparticles

AuNPs were characterized using ultraviolet-visible (UV/vis) absorption spectroscopy, dynamic light scattering (DLS), zeta potential (ζ-potential) measurements, scanning electron microscopy (SEM), and transmission electron microscopy (TEM).

UV/Vis spectra were acquired on an Agilent Varian Cary 50 Bio spectrophotometer using a 750 μL quartz cuvette with a 10 mm optical path length, pre-cleaned with aqua regia ($HNO_3$ : HCl, 1 : 3 v/v). Bare AuNPs were characterized by mixing 120 μL of AuNPs with 380 μL of ultrapure water. For functionalized AuNPs, 120 μL of AuNPs were mixed with 7 μL of citrate buffer (pH 6.0), 2 μL of peptide (P44-WT, P44-T, or P44-N), and 16 μL of MBA, then diluted with 355 μL of ultrapure water.

For serum interaction studies, 120 μL of AuNPs were combined with 7 μL of buffer, 2 μL of peptide, 16 μL of MBA, and 5 μL of serum (positive or negative), and then the volume was adjusted to 350 μL with ultrapure water.

For DLS and ζ-potential characterization, bare AuNPs were diluted by adding 10 μL of colloid to 990 μL of ultrapure water. Functionalized samples were prepared by mixing 120 μL of AuNPs, 7 μL of buffer, 2 μL of peptide, 16 μL of MBA, and 5 μL of ultrapure water. After conjugation, 10 μL of this mixture was diluted in 990 μL of ultrapure water. The same procedure was repeated, substituting 5 μL of water with 5 μL of either positive or negative serum to evaluate changes in hydrodynamic size and surface charge following antibody interaction. DLS and ζ-potential measurements were performed using a Malvern Zetasizer Nano ZS (Malvern Instruments, UK).

Scanning electron microscopy (SEM) analyses were performed on a field emission scanning electron microscope (FESEM) under ultra-high vacuum, model JMS-6701F (JEOL). For imaging, 10 μL of functionalized nanoparticle suspension was drop-cast onto a 4 × 4 mm silicon substrate fragment and dried at ambient conditions.

Transmission electron microscopy (TEM) and high-resolution TEM (HRTEM) images were acquired using a Talos F200X G2 (ThermoScientific) transmission electron microscope, equipped with a cold field emission gun (FEG-X) and scanning transmission electron microscopy (STEM) module, operated at 200 kV. Samples were prepared by drop-casting 5 μL of colloid onto carbon-coated copper grids and air-dried before imaging. Particle size distribution histograms were obtained by analyzing at least 100 particles using ImageJ software.

### SERS analysis and data processing

The custom-built sample support was first analyzed to verify potential interaction between the material and the laser. As a control, 150 μL of ultrapure water was pipetted onto the support and analyzed. All functionalization procedures for the AuNPs were carried out in 2 mL microcentrifuge tubes, where the reagents were combined in the specified volumes and gently homogenized.

For each SERS measurement, 145 μL of the functionalized AuNP solution was deposited in the support well. Then, 5 μL of ultrapure water was added for the blank condition (bare AuNPs), maintaining a constant final volume. The measurement was done by positioning the Raman probe directly above the well. The procedure was repeated in an adjacent well for the experimental samples, replacing the 5 μL of ultrapure water

with 5 μL of the previously diluted serum sample. Spectral acquisition was performed after a one-minute stabilization period, allowing for molecular interactions to occur.

The spectra were processed using MATLAB version 9.6.0.1072779 (R2019a). Initially, all data were labeled as "positive" or "negative" and preprocessed using a Whittaker filter ($\lambda$ = 1000, $\rho = 10^{-4}$) to reduce background noise and enhance signal quality. Data analysis was performed using PCA and PLS-DA methods through the PLS Toolbox 9.2 (2023) from Eigenvector Research, Inc.

Before classification, outliers were identified and removed using exploratory principal component analysis (PCA). The retained data were then mean-centered. PCA was employed to assess intrinsic sample distribution and variability, then a supervised classification model was constructed using partial least squares discriminant analysis (PLS-DA). The dataset was randomly divided into two subsets: ~70% for model training and ~30% for external validation.

Model performance was assessed through figures of merit, including sensitivity, specificity, and calibration/validation errors. Internal validation was performed using the leave-one-out cross-validation method to estimate model robustness and generalization capacity.

## Results and discussion

To optimize the biosensor's performance, the functionalization conditions of AuNPs were systematically evaluated, with a particular focus on the effects of solution pH and peptide concentration (Fig. S2). These parameters were shown to significantly influence the stability of the conjugates and the intensity of the SERS signal. The optimal condition was established at pH 6.0 in phosphate buffer, with a peptide concentration of 0.045 mg $L^{-1}$. Furthermore, including 0.04 mg $L^{-1}$ of MBA was essential for stabilizing the colloidal solution and enhancing the signal intensity, likely due to its role in improving the peptide's surface adsorption and Raman signal amplification.

The optimization process was supported by an analysis of variance (ANOVA), summarized in Table 1. The model yielded a coefficient of determination ($R^2$) of 71.10%, indicating that the proposed conditions explain a substantial portion of the data variability. The calculated *F*-value for the regression was higher than the tabulated *F*-value (*p*-value $< 0.05$), confirming the model's statistical significance. Meanwhile, the lack-of-fit *F*-value was lower than the critical threshold (*p*-value $> 0.05$), indicating that the model fits the experimental data well and does not exhibit a significant lack of fit. These results validate the experimental design and support the reliability and sensitivity of the optimized biosensor configuration for practical applications.

With the optimized parameters established, AuNPs conjugated with the peptides were characterized using UV-vis spectroscopy (Fig. S3) and DLS (Fig. S4). Previous studies have demonstrated that peptide conjugation causes a bathochromic shift in the plasmonic absorption band of AuNPs, indicating changes in the local electronic environment resulting from surface modification.[35,36] In our case, the spectra in Fig. S2 and S3 confirm that pH adjustment and peptide addition promoted successful conjugation, as indicated by the redshift in the LSPR band, characteristic of AuNP + peptide complexes.

Table 1 Analysis of variance (ANOVA) for the DCCR model (rotational central composite design). The table summarizes the statistical parameters used to evaluate the significance of the factors involved in the biosensor optimization process, including degrees of freedom (DF), sum of squares (SS), mean square (MS), *F*-values, and *p*-values. The coefficient of determination ($R^2$ = 71.10%) indicates that the model explains a substantial portion of the variability in the data

| Source | DF | SS | MS | *F* Value | *p*-Value |
|---|---|---|---|---|---|
| Regression | 4 | $4.00 \times 10^{31}$ | $1.00 \times 10^{33}$ | 2.89 | 0.014 |
| Error | 12 | $1.33 \times 10^{30}$ | $1.11 \times 10^{29}$ | — | — |
| Lack-of-fit | 10 | $1.23 \times 10^{30}$ | $1.23 \times 10^{29}$ | 2.49 | 0.32 |
| Pure error | 2 | $9.92 \times 10^{28}$ | $4.96 \times 10^{28}$ | — | — |
| Total | 16 | $1.73 \times 1030$ | — | — | — |

Conjugation was further supported by DLS measurements, which showed an increase in hydrodynamic radius ($R_H$) following peptide attachment (Fig. 2 and Fig. S4). This increase is attributed to the formation of a hydration shell around the AuNPs due to biomolecular adsorption, which alters their diffusion behavior in solution.[37,38] DLS is particularly suitable for detecting such nanoscale interactions, offering insights into molecular binding and aggregation phenomena, especially in biologically complex environments.[39–41]

When exposed to serum samples, distinct $R_H$ patterns were observed depending on the presence or absence of SARS-CoV-2 antibodies (Fig. 2, Fig. S4; Table 2). Negative sera induced minimal changes in LSPR and $R_H$, consistent with non-specific interactions. In contrast, convalescent serum led to a pronounced increase in $R_H$ and redshift of the plasmonic band, indicative of aggregate formation mediated by antibody–peptide recognition. SEM images further confirmed these interactions for the P44-WT peptide (Fig. 2), showing clear morphological changes only in the presence of both the peptide and specific antibodies. The data reinforce the conclusion that specific biomolecular recognition events predominantly drive aggregation.

In addition to the UV-vis and DLS characterization, zeta potential measurements were performed to assess further peptide adsorption and the impact of serum incubation on the nanoparticle surface charge (Fig. S5). The $\zeta$-potential of citrate-stabilized AuNPs was initially $-35.6 \pm 2.3$ mV, indicating a highly stable colloidal suspension. Upon conjugation with the P44-WT peptide, this value shifted to $-23.1 \pm 1.8$ mV, consistent with partial neutralization of surface charge. After incubation with convalescent serum (positive for SARS-CoV-2 antibodies), a further shift to $-14.7 \pm 1.5$ mV was observed, reflecting antibody binding and protein corona formation. These findings corroborate the spectroscopic and DLS results, confirming successful surface functionalization and specific biomolecular interactions.

To further validate peptide conjugation onto the AuNP surface, TEM analyses were performed. The images revealed a contrast

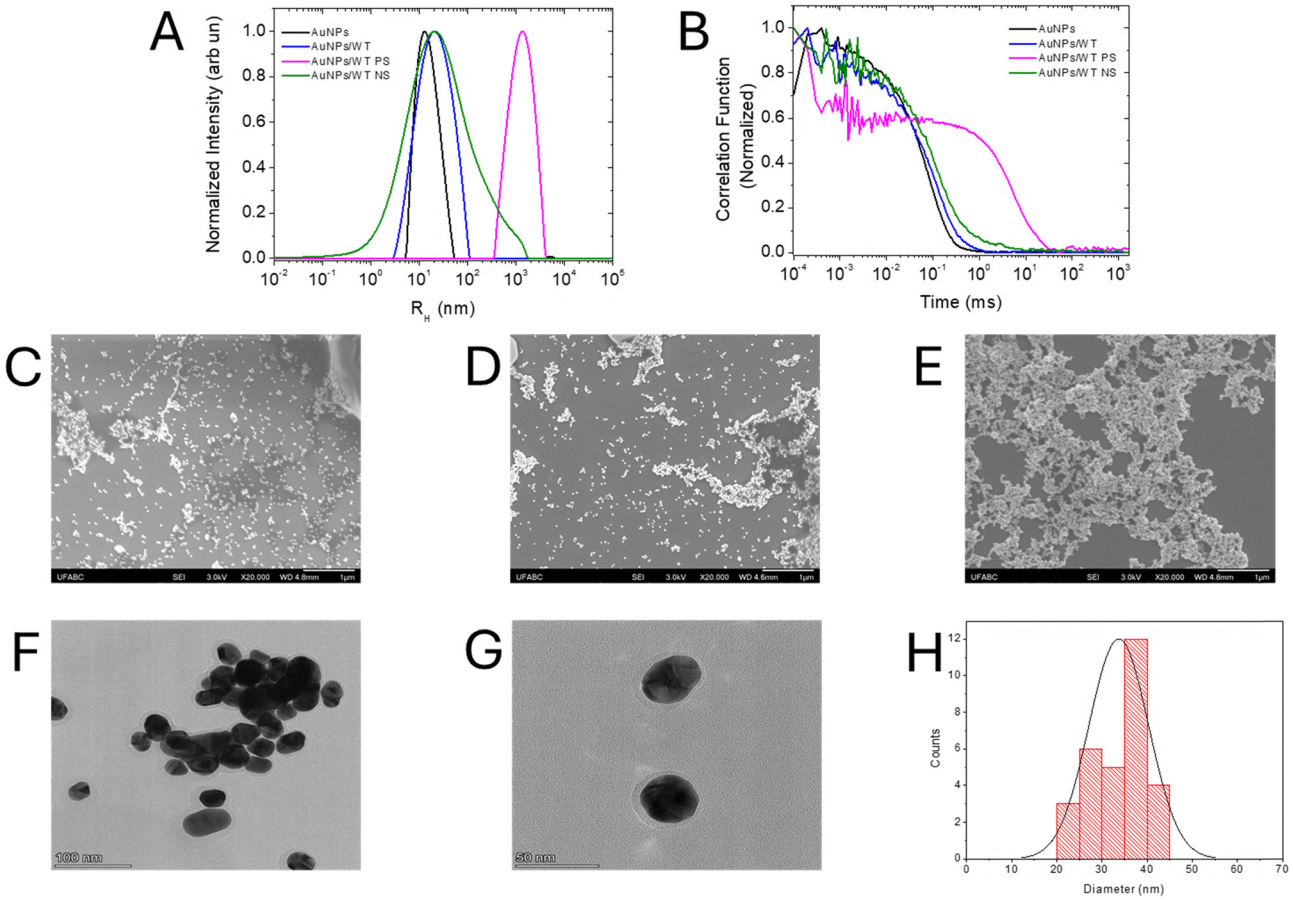


Fig. 2 Characterization of AuNPs before and after functionalization with the P44 peptide and their interaction with SARS-CoV-2 positive serum samples. (A) DLS particle size distribution; (B) DLS cumulative intensity plot; SEM images of (C) unmodified AuNPs, (D) AuNPs functionalized with P44, and (E) AuNPs/P44 incubated with SARS-CoV-2 positive serum; (F) TEM image of unmodified AuNPs; (G) TEM image of AuNPs functionalized with P44; (H) histogram of core size distribution obtained from TEM analysis.

Table 2 Characterization parameters of AuNPs before and after functionalization, including hydrodynamic radius ($R_H$), polydispersity index (PDI), and localized surface plasmon resonance (LSPR) values. Data are shown for different peptides and in the presence of complex serum samples. PS = positive serum (convalescent samples positive for SARS-CoV-2 antibodies); NS = negative serum (pre-pandemic samples with no SARS-CoV-2 exposure)

| Samples | $R_H$ (nm) | PDI | LSPR |
|---|---|---|---|
| AuNPs | 11.75 | 0.337 | 532 |
| AuNPs/WT | 15.89 | 0.480 | 535 |
| AuNPs/WT PS | 937.68 | 0.383 | 626 |
| AuNPs/WT NS | 22.76 | 0.497 | 540 |
| AuNPs/N | 50.41 | 0.326 | 650 |
| AuNPs/N PS | 1027.49 | 0.100 | 535 |
| AuNPs/N NS | 11.92 | 0.362 | 536 |
| AuNPs/T | 51.17 | 0.349 | 535 |
| AuNPs/T PS | 861.95 | 0.420 | 666 |
| AuNPs/T NS | 15.82 | 0.496 | 536 |

halo around the peptide-functionalized nanoparticles (Fig. 2F and G), which was absent in the unmodified AuNPs (Fig. S6), indicating the presence of an organic layer attributed to the adsorbed peptide. The corresponding size distribution histogram (Fig. 2H) confirmed a narrow size dispersion, consistent with the average core diameter measured by TEM, further supporting the uniformity of the synthesized nanoparticles. These results reinforce the successful surface modification and support the observations obtained from DLS, zeta potential, and UV-vis analyses.

Over time, the system exhibited visible precipitation upon exposure to positive serum, accompanied by a notable LSPR shift, further $R_H$ increase, and a color transition of the colloid from red to purple—hallmarks of nanoparticle aggregation. This aggregation decreases interparticle distance, creating nanogaps and interstitial sites that significantly enhance the local electromagnetic field. As a result, the SERS signal is significantly amplified.[42]

Although aggregation may affect colloidal stability, it is a favorable phenomenon in this context as it enhances the biosensor's sensitivity. The increased proximity of nanoparticles improves molecular confinement and signal amplification, particularly in the presence of specific serum antibodies. These findings underscore the importance of thoroughly understanding the dynamic interactions between functionalized nanoparticles and biological components, which are essential for designing sensitive and reliable biosensing platforms.[43]

MBA also played a key role in enhancing the quality of the Raman spectrum, functioning as a molecular probe within the active substrate and contributing to more precise molecular identification.[31–34] Its effectiveness stems from a symmetry-breaking effect, which alters the intensity ratio between specific aromatic ring vibrational modes, thereby improving spectral resolution.[32] Notably, the intensity and shape of characteristic MBA bands, such as those at 1021 and 988 $cm^{-1}$, are influenced by the pH of the medium, indicating that the molecule is sensitive to environmental conditions.[44]

To investigate spectral differences associated with each peptide variant, principal component analysis (PCA) was applied to the SERS data (Fig. 3). This multivariate technique reduces data dimensionality, enabling pattern recognition and clustering based on subtle spectral variations. The classification performance was further refined using partial least squares-discriminant analysis (PLS-DA), a supervised method particularly suited for datasets with high collinearity, such as Raman-SERS spectra (Fig. 4). PLS-DA facilitates model calibration and enhances classification accuracy by maximizing the covariance between spectral features and class labels.

The results obtained with the P44-WT peptide were particularly robust (Fig. 3, 4, and Fig. S7; Table 3). In the PCA plot (Fig. 3A), the negative serum samples formed a well-defined cluster along the positive axis of PC2. The corresponding loading plot (Fig. 3B) revealed that this separation was predominantly influenced by a vibrational mode at approximately 770 $cm^{-1}$. In contrast, the positive serum samples exhibited greater dispersion, spreading mainly along PC1, suggesting spectral heterogeneity associated with specific molecular interactions. The high classification accuracy observed for P44-WT confirms the biosensor's effectiveness in detecting this variant. However, for the P44-T and P44-N mutant peptides, although sensitivity remained relatively high, specificity was reduced. This reduction may be attributed to structural modifications in the peptide sequences resulting from point mutations, which likely affected biosensor stability and peptide–antibody binding affinity.[45]

These findings validate the applicability of Raman-SERS spectroscopy combined with multivariate analysis for detecting SARS-CoV-2 antibodies. They also emphasize the importance of tailoring biosensor design to accommodate sequence-specific differences across viral variants, thereby maximizing analytical performance.

Altogether, PCA and PLS-DA were essential tools for evaluating the discriminatory capacity of the SERS biosensor platform, successfully differentiating between samples from infected and non-infected individuals based on molecular signatures. These results demonstrate the robustness of the analytical model and its potential in the variant-specific identification of SARS-CoV-2.

In addition to the spectroscopic results, electrochemical experiments were performed using the same peptides—P44-WT, P44-T, and P44-N—as shown in Fig. 5. Electrochemical impedance spectroscopy (EIS) was employed as a complementary and highly

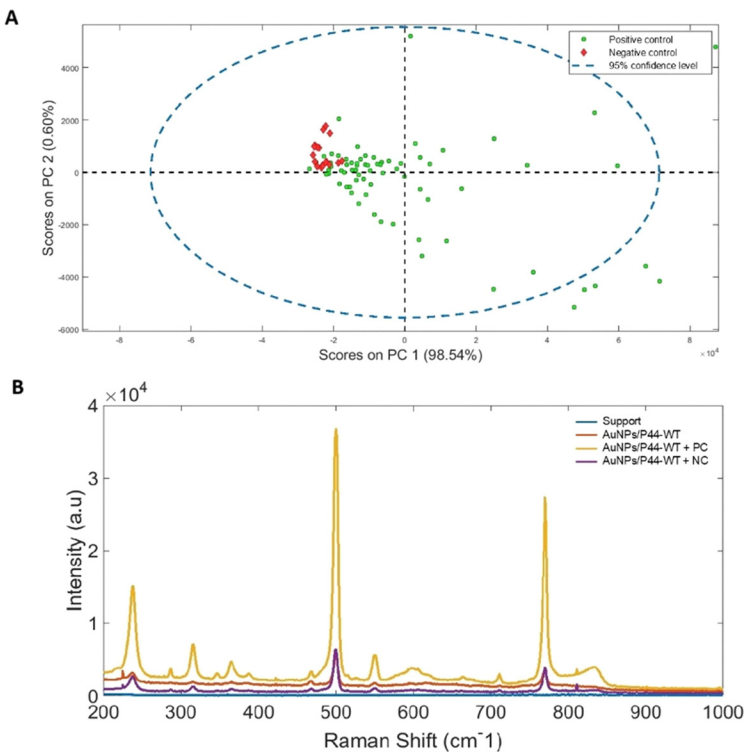


Fig. 3 Raman spectral analysis for differentiating SARS-CoV-2 positive and negative serum samples. (A) Principal component analysis (PCA) score plot of PC1 *versus* PC2, highlighting the separation between positive and negative controls within the 95% confidence ellipse. (B) SERS spectra under different conditions: blue = instrumental support (blank, without sample); red = substrate functionalized with P44-WT; yellow = P44-WT incubated with positive control (PC) serum; purple = P44-WT incubated with negative control (NC) serum.

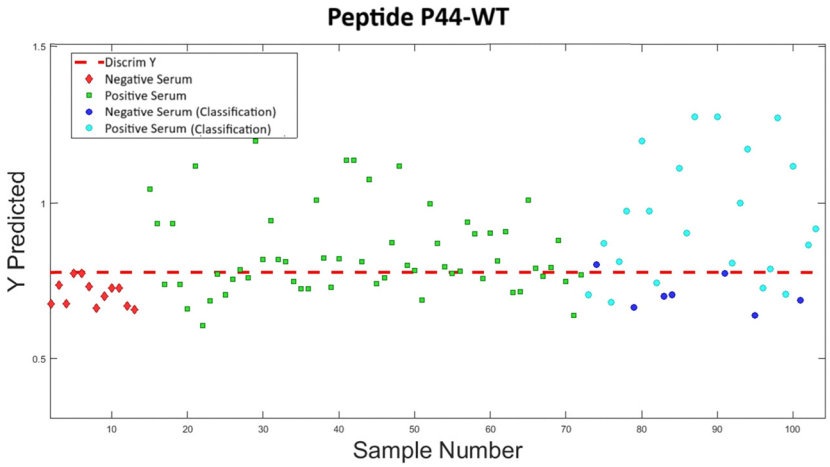


Fig. 4 PLS-DA classification of SARS-CoV-2-specific serum antibodies using the P44-WT peptide-based biosensor. Samples below the threshold (dashed red line) are classified as negative, while those above are classified as positive. The plot illustrates the model's performance in discriminating between positive and negative serum samples based on antibody recognition against the P44-WT peptide.

Table 3 Performance metrics of the PLS-DA classifier for discriminating SARS-CoV-2 positive and negative serum samples, including sensitivity, specificity, and Matthew's correlation coefficient (MCC)

| | P44-WT | | | P44-T | | | P44-N | | |
|---|---|---|---|---|---|---|---|---|---|
| Parameters | Calibration | Cross validation | Test | Calibration | Cross validation | Test | Calibration | Cross validation | Test |
| Sensitivity | 100 | 92.3 | 100.0 | 85.0 | 75.0 | 90.0 | 82.4 | 64.7 | 63.6 |
| Specificity | 88.9 | 75.6 | 75.6 | 70.7 | 70.7 | 62.5 | 75.9 | 74.1 | 63.2 |
| MCC | 0.89 | 0.69 | 0.78 | 0.55 | 0.44 | 0.53 | 0.58 | 0.39 | 0.27 |

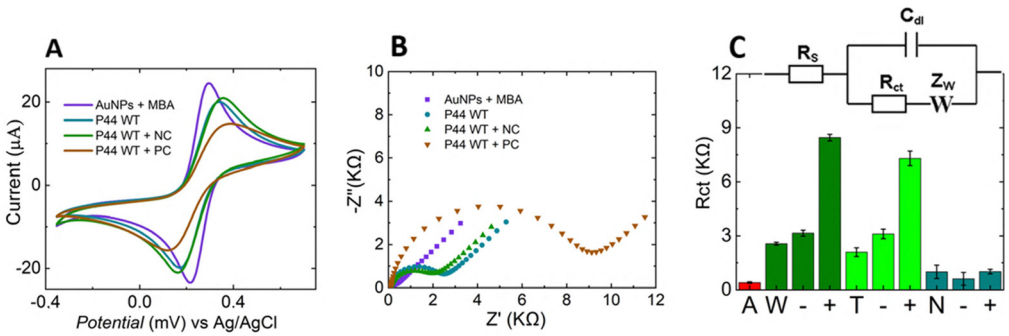


Fig. 5 Electrochemical characterization of AuNP–peptide biosensors in the presence of serum samples from SARS-CoV-2 positive (PC) and negative (NC) patients. (A) Cyclic voltammetry (CV), (B) electrochemical impedance spectroscopy (EIS), and (C) charge transfer resistance ($R_{ct}$) values obtained from Randles circuit fitting. In panel (C), A = AuNPs + MBA (blank), W = P44-WT, T = P44-T, and N = P44-N, with "+" indicating positive serum and "−" indicating negative serum. Inset: Randles equivalent circuit used for fitting. Electrolyte: 5 mmol $L^{-1}$ $[Fe(CN)_6]^{3-/4-}$ in 0.1 mol $L^{-1}$ KCl.

sensitive technique to monitor biomolecular interactions. EIS allows real-time detection under near-physiological conditions and is compatible with a wide range of materials, making it suitable for miniaturization and integration into rapid diagnostic platforms.[46]

These experiments also aimed to validate the classification capability observed in the PLS-DA models generated from the SERS data. By applying the same peptides in electrochemical biosensors, the impedance measurements provided quantitative insights into critical performance parameters, including selectivity, specificity, and sensitivity. Such metrics are fundamental for ensuring the reliability of biosensors in clinical diagnostics.[11,47]

The same peptide-functionalized solutions used in the SERS assays were deposited onto glassy carbon electrodes (GCEs) and analyzed by cyclic voltammetry (CV) and EIS, using the redox couple potassium ferrocyanide/ferricyanide ($K_4Fe(CN)_6$/$K_3Fe(CN)_6$) in potassium chloride as the supporting electrolyte. The results obtained for the P44-WT (Fig. 5A and B), P44-T (Fig. S8A and B), and P44-N (Fig. S8C and D) peptides are summarized in the bar graph presented in Fig. 5C, based on data extracted from fitting with the Randles equivalent circuit.

It is well established that GCE modification with AuNPs can be achieved through a simple drop-casting method, followed by

adsorption *via* electrostatic interactions.[11] The initial presence of AuNPs enhances the charge transfer process due to their intrinsic conductivity.[48] In acidic media, AuNPs deposited on GCEs produced well-defined redox peaks corresponding to the electrochemical probe (Fig. 5A), along with a small semicircle in the Nyquist diagram indicative of low charge transfer resistance ($R_{ct} \sim 400\ \Omega$, Fig. 5B), further confirming their conductive behavior.

Upon the addition of peptide-conjugated AuNPs, a decrease in the intensity of the redox peaks was observed, indicating successful peptide conjugation and subsequent adsorption onto the electrode surface. The AuNPs synthesized *via* citrate reduction exhibit a net negative surface charge, conferring stability and reactivity in biological environments. Meanwhile, the ferrocyanide/ferricyanide probe, being negatively charged, normally facilitates charge transfer across bare or citrate-stabilized AuNP-modified electrodes.[49]

Following peptide conjugation, citrate ions are replaced by peptide molecules that act as stabilizing ligands. However, this substitution reduces the surface charge density and introduces a steric barrier, which hinders electron transfer. Consequently, a decrease in redox peak intensity, a shift to more positive potentials (Fig. 5A), and an increase in the $R_{ct}$ value to approximately 2600 Ω (Fig. 5B) were observed. These changes reflect a reduced dielectric constant at the electrode interface and lower electron transfer efficiency due to the insulating nature of the immobilized peptides.[50–53] This behavior was consistently observed for all three peptide variants tested, as shown in Fig. S8.

No significant changes were observed in the electrochemical response after adding the negative control (plasma samples from pre-pandemic individuals). This outcome aligns with expectations, as these samples are unlikely to contain antibodies that can specifically bind to the functionalized peptides. The minor variations detected may be attributed to nonspecific interactions or background noise inherent to the complexity of the biological matrix. These findings support the specificity of the biosensor, indicating that the system selectively responds to the presence of antibodies generated against SARS-CoV-2.

In the presence of positive control (plasma from convalescent COVID-19 patients), a 93% increase in $R_{ct}$ values was observed for the P44-WT peptide. This significant shift is attributed to the binding of circulating antibodies to the functionalized surface, confirming that the system is selective and capable of recognizing the target analyte even in a complex biological matrix. These antibodies, which bind to the peptides conjugated to the AuNPs, are largely insulated in nature due to their glycoprotein composition. Their adsorption onto the electrode surface impedes the charge transfer of the redox probe, resulting in reduced peak intensity in the voltammograms and elevated $R_{ct}$ values in the Nyquist plots.

Previous studies have shown that the molecular architecture of antibodies, particularly the presence of glycosylated Fc domains and variable regions, contributes to their insulating behavior by limiting electronic interactions.[54,55] These structures, composed of protein subunits and carbohydrate moieties, act as physical and electrochemical barriers restricting electron flow, a property that must be considered in biosensor design.

Comparison of results obtained in the microarray chip for P44 WT and data obtained from the biosensor showed a strong correlation between microarray and EIS data (Fig. S9), confirming that the biosensor signals reflect specific antibody binding. The mutated peptides were designed based on literature evidence indicating reduced antibody affinity for these variants.[26,56] The biosensor's ability to detect this expected decrease in binding further supports its specificity and reliability.

When evaluating the mutant peptides P44-T and P44-N, a notable reduction in signal response was observed, indicating impairments in the immobilization of the peptide on the electrode surface and its recognition by specific antibodies. Nonetheless, both mutant systems were still able to discriminate between positive and negative samples. Quantitatively, decreases of 18% and 75% in the immobilization process, and 13% and 88% in antibody detection, were recorded for P44-T and P44-N, respectively.

These observations align with evidence that variants of concern (VOCs) associated with increased transmissibility often exhibit reduced recognition by neutralizing antibodies (nAbs) in individuals who have recovered from the disease.[57] This reduced binding is frequently linked to point mutations in the Spike protein's receptor-binding domain (RBD), which alter critical epitopes.[25] For instance, in the South African (beta, P44-N) variant, the substitution of lysine by asparagine significantly modifies the local protein structure, impairing antibody binding and reducing surface retention. Conversely, the gamma variant (P44-T), which involves the substitution of lysine by threonine, induces a less drastic conformational change, preserving a higher degree of antibody recognition.

These findings reinforce the importance of carefully selecting the immunogenic peptide for biosensor construction, as mutations may compromise antigen–antibody interactions, ultimately affecting sensitivity and specificity.[26]

The calibration curves and the analysis using serum from both COVID-19 convalescent patients and SARS-CoV-2-negative individuals are presented in Fig. 6. This study demonstrates the biosensor's capacity to operate effectively in complex biological matrices, confirming its applicability in real clinical samples. The system's ability to reliably distinguish between positive and negative cases underscores the sensitivity and specificity of the developed biosensor.

The employed methodology enabled the detection of SARS-CoV-2 antibodies at very low concentrations, yielding limits compatible with clinical diagnostic requirements. The analysis of convalescent serum samples confirmed that the selected immunodominant peptides exhibit high affinity toward antibodies elicited by SARS-CoV-2 infection, enabling accurate identification of positive cases.

Calibration curves were constructed using the monoclonal antibody B38 (anti-SARS-CoV-2), a purified antibody free from contaminants or interfering agents. The resulting detection limits were 0.43 ng $mL^{-1}$, 4.85 ng $mL^{-1}$, and 8.04 ng $mL^{-1}$ for the peptides P44-WT, P44-T, and P44-N, respectively.

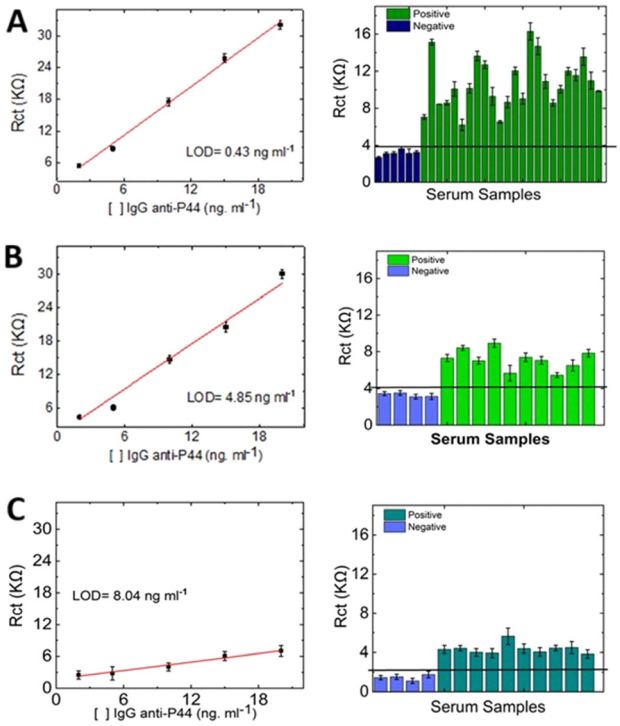


Fig. 6 Calibration curves and analytical performance of peptide-based biosensors tested with serum samples from convalescent SARS-CoV-2 patients and negative controls. (A) Biosensor functionalized with P44-WT; (B) P44-T; and (C) P44-N. Left panels: Calibration plots of charge transfer resistance ($R_{ct}$) *versus* anti-P44 IgG concentration (ng $mL^{-1}$), with limits of detection (LOD) indicated. Right panels: $R_{ct}$ values obtained for individual serum samples, determined by fitting to the Randles equivalent circuit. Electrolyte: 5 mmol $L^{-1}$ $[Fe(CN)_6]^{3-/4-}$ in 0.1 mol $L^{-1}$ KCl.

These values indicate that all peptides tested exhibit suitable biorecognition capabilities, with detection thresholds in the nanogram range, which is adequate for biosensing applications.

However, the calibration curves and response patterns shown in Fig. 6 reveal that mutations in the peptide sequence negatively influence sensitivity. Although P44-T and P44-N retained their ability to discriminate between positive and negative samples, their overall signal intensities were reduced, reflecting a diminished affinity or recognition efficiency. Despite this decline, no interference was observed from serum components, indicating that the functionalized bioelectrodes were resistant to biofouling and nonspecific adsorption.[48] These findings support the robustness and specificity of the biosensor platform, even in complex media.

The T variant (P44-T) exhibits a transmissibility rate 1.4 to 2.5 times higher than that of the ancestral SARS-CoV-2 strain (WT), along with a 25% to 61% probability of evading protective immunity elicited by prior infection or vaccination. Similarly, the South African variant (P44-N) shows increased transmissibility and an even greater capacity to escape immune recognition.[26,56,58] These characteristics illustrate how viral mutations can simultaneously enhance transmissibility and hinder the detection of specific targets—an effect reflected in the performance of the biosensors developed in this study. The ability of such variants to evade immunity underscores the need for robust and adaptable platforms that can rapidly detect evolving viral strains and track the dynamics of SARS-CoV-2 mutations.

Marked differences were observed among the peptides tested, with P44-WT consistently yielding the best analytical responses, followed by P44-T and P44-N, across both biosensing platforms. This trend aligns with expectations from published structural and immunological studies of SARS-CoV-2 antibody recognition, as the serum samples were collected during the early pandemic phase when the ancestral (WT) strain exclusively caused infections. Previous work has demonstrated that this single-amino acid substitution in this epitope region reduced antibody binding affinity,[26,56] consistent with our observations. The biosensor data thus reflect the expected immune recognition patterns for this cohort. Additionally, biosensor optimization procedures, such as adjusting the buffer pH, were conducted using the P44-WT peptide, which may have contributed to its superior performance. Given the distinct isoelectric points of the peptides, it is possible that the buffer condition (pH 6.0) was not optimal for the mutant variants, which could have affected their recognition efficiency.[59]

These findings highlight the importance of considering peptide-specific physicochemical properties during biosensor development to ensure high specificity and sensitivity. Ongoing studies aim to elucidate further how specific mutations influence the recognition of neutralizing antibodies.

To better summarize the practical and analytical performance of the two biosensing approaches developed in this study, Table 4 provides a comparative overview of the SERS and EIS platforms. The limits of detection (LODs) achieved for the P44-WT, P44-T, and P44-N peptides were 0.43 ng $mL^{-1}$, 4.85 ng $mL^{-1}$, and 8.04 ng $mL^{-1}$, respectively. These values demonstrate that the proposed peptide-based biosensors are highly competitive with or superior to several previously reported devices for detecting anti-SARS-CoV-2 antibodies.

For instance, Castro *et al.* (2022) developed an electrochemical biosensor using a synthetic Spike-derived peptide, which achieved an LOD of 1.5 ng $mL^{-1}$.[11] Similarly, Braz *et al.* (2022) reported a sensor employing a fusion of a graphene-binding peptide and Spike antigen with a significantly higher LOD of 770 ng $mL^{-1}$, indicating lower sensitivity.[60] Nunez *et al.* (2023) developed a ZnONRs-based immunosensor functionalized with monoclonal antibodies that achieved an LOD of 10 ng $mL^{-1}$,[9] while Nicoliche *et al.* (2022) reported a paper-based electrochemical biosensor with antifouling nanocoating, reaching an LOD of 4.0 ng $mL^{-1}$ in serum.[48] Hryniewicz *et al.* (2022) introduced an impedimetric biosensor using polypyrrole nanotubes decorated with gold nanoparticles, which enabled the sensitive and label-free detection of anti-SARS-CoV-2 IgG antibodies in clinical serum samples, with an LOD of 0.4 ng $mL^{-1}$ and 90% sensitivity in ROC analysis.[61] More recently, a study from our group demonstrated that adapting the ZnONRs-based platform with Spike proteins from both the wild-type and gamma variant allowed accurate serological profiling of vaccine-induced immunity.[62] These findings reinforce the superior sensitivity of our peptide-based platforms, particularly the P44-WT

Table 4 Comparative analytical and operational characteristics of SERS- and EIS-based biosensors developed with the P44 peptide

| Feature | SERS biosensor | Electrochemical biosensor (EIS) |
|---|---|---|
| Best-performing peptide | P44-WT | P44-WT |
| Sensitivity (P44-WT) | 100% | High (93% increase in $R_{ct}$) |
| Specificity (P44-WT) | 76% | Not explicitly modeled, but high |
| Limit of detection (LOD) | Not defined (classification-based) | 0.43 ng mL$^{-1}$ (WT), 4.85 (T), 8.04 (N) |
| Effect of mutations (T/N) | Reduced spectral discrimination | Reduced signal and increased LOD |
| Matrix compatibility | High (serum with minimal interference) | High (serum with minimal interference) |
| Portability | High (Raman-based, potential POC) | Moderate (lab bench setup) |
| Operational simplicity | Requires a Raman reader | Simple electrode setup |
| Quantification capability | Limited (PLS-DA-based discrimination) | Strong (direct measurement *via* $R_{ct}$) |

variant, which outperformed most comparable platforms in terms of detection sensitivity.

In addition to enhanced sensitivity, our biosensor demonstrated the capability to differentiate antibodies against specific variants through the use of mutation-specific peptides (P44-T for gamma and P44-N for beta). While the LODs for these variant-specific peptides were slightly higher than those of P44-WT, they remained in the low nanogram-per-milliliter range, outperforming most sensors based on structurally complex proteins or fusion constructs.

A key advantage of our platform is its robust analytical performance in untreated human serum samples, requiring no additional preprocessing. This represents a significant improvement over protein-based biosensors, which often suffer from stability issues, batch-to-batch variability, and higher production costs. Furthermore, the SERS-based method demonstrated 100% sensitivity and 76% specificity using PLS-DA, results that are comparable to or exceed those reported in the literature, where sensitivity values typically range from 90% to 100% and specificity frequently drops below 85%.

Collectively, these results confirm the efficacy of short synthetic peptides, such as the immunodominant P44, as highly stable, scalable, and mutation-responsive biorecognition elements. Their integration into electrochemical and spectroscopic biosensing platforms offers a robust and flexible approach for ongoing SARS-CoV-2 immune surveillance and may be adapted for monitoring responses to other emerging viral pathogens.

In this context, peptide-based electrochemical biosensors represent a promising strategy, as they can be readily updated by selecting variant-specific peptide sequences. EIS offers a reliable and accurate platform for detecting both the wild-type virus and its variants.[63] Additionally, multivariate analysis using PLS-DA applied to SERS data confirmed the high sensitivity and specificity of this approach, validating its use in complex biological matrices.

Both techniques, SERS and EIS, demonstrated distinct advantages in terms of sensitivity, speed, and specificity. SERS enables high-resolution molecular fingerprinting and rapid data acquisition, while EIS provides precise quantitative analysis and real-time monitoring of biomolecular interactions. Importantly, the modular nature of peptide-based biosensors allows for rapid reconfiguration to accommodate the evolving mutational landscape of the virus, supporting broader applicability in diagnosing other emerging infectious diseases.

In summary, this study evaluated the analytical performance of peptide-functionalized SERS and EIS biosensors for detecting antibodies against SARS-CoV-2, with a focus on immunodominant epitopes derived from both wild-type and variant Spike protein sequences. Among the tested peptides, P44-WT yielded the most favorable results, followed by P44-T and P44-N. Both biosensing techniques presented valuable features: SERS enabled ultrasensitive and portable detection, though with higher instrumentation costs, while EIS offered a simpler, cost-effective, and robust alternative suitable for routine diagnostics.

The intended application should guide the choice between platforms: SERS is better suited for high-throughput or point-of-care scenarios, whereas EIS is ideal for centralized laboratory settings requiring accurate quantification. Continued innovation in peptide-based biosensing platforms remains essential to strengthen pandemic preparedness. Ultimately, the use of short synthetic peptides as biorecognition elements outperformed full-length Spike proteins in terms of signal-to-noise ratio, stability, and reproducibility, reinforcing their value for scalable, variant-resilient immune monitoring. These findings position peptide biosensors as practical tools for population-level surveillance and future diagnostic strategies in rapidly evolving viral outbreaks.

## Conclusions

This study demonstrated the effectiveness of biosensors based on SERS and EIS for detecting SARS-CoV-2 antibodies using the immunodominant peptide P44 and its mutated variants. Among the peptides tested, P44-WT demonstrated superior performance across both platforms, achieving 100% sensitivity and 76% specificity in SERS and a detection limit of 0.43 ng mL$^{-1}$ in EIS. These outcomes reflect the optimized experimental conditions (pH 6.0) and the predominance of antibodies targeting the ancestral viral strain in the analyzed serum samples.

The comparative analysis of both techniques highlighted their complementarity: SERS enabled rapid, ultrasensitive, and portable detection with molecular specificity, while EIS provided a cost-effective and operationally simple approach, particularly suited for quantitative analyses in laboratory environments. Both systems effectively differentiated between positive and negative samples, maintaining high performance in

 

complex biological matrices with negligible interference from serum components.

The study also revealed that point mutations in the P44 peptide, corresponding to the gamma (P44-T) and beta (P44-N) variants, negatively affected biosensor sensitivity and peptide immobilization. Despite these challenges, both variants remained capable of distinguishing infected from non-infected samples. These findings highlight the importance of meticulous peptide selection and optimization in biosensor development, particularly when targeting rapidly evolving viral strains.

Future adaptations of this platform may benefit from tailored optimization of physicochemical parameters, such as pH, ionic strength, and surface modification strategies, according to the specific properties of each variant-derived peptide. Such refinements could enhance biosensor performance and adaptability in response to emerging variants.

In conclusion, this work supports using peptide-based biosensing platforms as flexible, scalable, and high-performance tools for immunosurveillance in diagnosing infectious diseases. Their modular architecture and capacity to incorporate updated immunodominant sequences make them valuable assets for large-scale surveillance and rapid response in public health, particularly when integrated into portable, point-of-care diagnostic systems.

## Author contributions

Amanda E. Sabaine: conceptualization, data curation, formal analysis, investigation, methodology, validation, visualization, writing – original draft, writing – review & editing. Ana C. H. Castro-Kochi: conceptualization, data curation, formal analysis, investigation, methodology, project administration, supervision, validation, visualization, writing – original draft, writing – review & editing. Rodrigo S. N. Mancini: conceptualization, formal analysis, investigation, methodology, writing – original draft, writing – review & editing. Marcos R. A. Silva: data curation, formal analysis, investigation, methodology, validation. Anderson F. Sepulveda: conceptualization, supervision, writing – review & editing. Jamille R. Oliveira: formal analysis, investigation, methodology, resources. Cesar Remuzgo: formal analysis, methodology, resources. Keity S. Santos: conceptualization, data curation, funding acquisition, methodology, project administration, resources, supervision, writing – original draft, writing – review & editing. Vivian L. de Oliveira: conceptualization, methodology, writing – original draft, writing – review & editing. Leandro T. Kochi: data curation, writing – review & editing. Lauro T. Kubota: conceptualization, funding acquisition, methodology, project administration, resources, supervision. Mónica B. Mámian-López: conceptualization, data curation, formal analysis, methodology, resources, supervision, writing – original draft, writing – review & editing. Wendel A. Alves: conceptualization, data curation, formal analysis, funding acquisition, methodology, project administration, resources, supervision, writing – original draft, writing – review & editing.

## Conflicts of interest

There are no conflicts to declare.

## Data availability

Supplementary information: Details of biosensor optimization, physicochemical characterization of peptide-functionalized AuNPs (UV-Vis, DLS, zeta potential, TEM), statistical analysis (PLS-DA), electrochemical assays (CV and EIS), and correlation with microarray/ELISA results. See DOI: **https://doi.org/10.1039/d5ma00485c**

The manuscript and its SI include all data supporting this study. Additional datasets generated and analyzed during this study are available from the corresponding author upon reasonable request.

## Acknowledgements

This work was supported by FAPESP (grants #2024/00989-7, #2022/14753-0 and #2014/50890-5), CNPq (grants #305574/2023-0, #152436/2022-7), and the National Institute of Science and Technology in Bioanalytics – INCTBio (CNPq grant #408338/2024-5). Additionally, this study was partially funded by the Coordination for the Improvement of Higher Education Personnel – Brazil (CAPES, Finance code 001). The authors are grateful to the Multiuser Central Facilities at UFABC.

## References

1 O. Filchakova, D. Dossym, A. Ilyas, T. Kuanysheva, A. Abdizhamil and R. Bukasov, *Talanta*, 2022, **244**, 123409.
2 V. S. Lima, S. T. B. Morais, V. G. Ferreira, M. B. Almeida, M. P. B. Silva, T. D. A. Lopes, J. M. de Oliveira, J. R. S. Raimundo, D. Z. S. Furtado and F. L. A. Fonseca, *ACS Omega*, 2024, **9**, 45746.
3 D. C. M. Ferreira, N. I. G. Inoque, A. A. Tanaka, L. M. F. Dantas, R. A. A. Muñoz and I. S. da Silva, *Anal. Methods*, 2024, **16**, 4136.
4 H. Zhang, N. Rafat, J. Rudge, S. P. Peddireddy, Y. N. Kim, T. Khan and A. Sarkar, *Anal. Methods*, 2024, **16**, 7854.
5 Q. Bayin, L. Huang, C. Ren, Y. Fu, X. Ma and J. Guo, *Talanta*, 2021, **227**, 122207.
6 P. Merino-Amador, P. González-Donapetry, M. Domínguez-Fernández, F. González-Romo, M. Á. Sánchez-Castellano, A. Seoane-Estevez, A. Delgado-Iribarren, J. García, G. Bou and M. Cuenca-Estrella, *J. Clin. Virol.*, 2021, **143**, 104961.
7 D. S. Rocha, T. A. Baldo, H. A. Silva-Neto, G. F. Duarte-Junior, G. S. Bazílio, C. L. Borges, J. A. Parente-Rocha, W. R. de Araujo, A. de Siervo and T. R. L. C. Paixão, *Talanta*, 2024, **268**, 125337.
8 A. Baskar, K. Madhivanan, R. Atchudan, S. Arya and A. K. Sundramoorthy, *Clin. Chim. Acta*, 2024, 120054.
9 F. A. Nunez, A. C. H. Castro, V. L. de Oliveira, A. C. Lima, J. R. Oliveira, G. X. de Medeiros, G. L. Sasahara, K. S. Santos,

A. J. C. Lanfredi and W. A. Alves, *ACS Biomater. Sci. Eng.*, 2022, **9**, 458.
10 R. S. N. Mancini, A. E. Sabaine, C. E. Castro, J. B. T. Carnielli, R. Dietze, V. L. de Oliveira, A. J. C. Lanfredi, L. T. Kubota, M. B. Mamian-Lopez and W. A. Alves, *ACS Appl. Electron. Mater.*, 2022, **4**, 3997.
11 A. C. H. Castro, Í. R. S. Bezerra, A. M. Pascon, G. H. Da Silva, E. A. Philot, V. L. De Oliveira, R. S. N. Mancini, G. R. Schleder, C. E. Castro and L. R. S. De Carvalho, *ACS Nano*, 2022, **16**, 14239.
12 F. A. Nunez, V. L. Oliveira, C. Remuzgo, M. R. A. Silva, I. Daher, J. R. Oliveira, T. L. Silva, E. Cunha-Neto, J. Kalil, K. S. Santos, Q. A. Besford and W. A. Alves, *J. Mater. Chem. B*, 2025, **13**, 9925.
13 V. R. Rodovalho, G. R. Araujo, E. R. Vaz, C. Ueira-Vieira, L. R. Goulart, J. M. Madurro and A. G. Brito-Madurro, *Biosens. Bioelectron.*, 2018, **100**, 577.
14 R. L. Karpel, M. S. Liberato, J. D. Campeiro, L. Bergeon, B. Szychowski, A. Butler, G. Marino, J. F. Cusic, L. C. G. Oliveira, E. B. Oliveira, M. A. Farias, R. V. Portugal, W. A. Alves, M.-C. Daniel and M. A. F. Hayashi, *Colloids Surf., B*, 2018, **163**, 1.
15 V. L. B. França, E. M. Bezerra, R. F. da Costa, H. F. Carvalho, V. N. Freire and G. Matos, *ACS Chem. Neurosci.*, 2024, **15**, 3543.
16 M. M. Hassan, Y. Xu, M. Zareef, H. Li and Q. Chen, *TrAC, Trends Anal. Chem.*, 2022, **156**, 116707.
17 B. Cao, P. Lin, Y. Wang, W. Yang, L. Ren, Z. Ge, H. Sui, Y. Gao, M. Liu and G. Bei, *Biosens. Bioelectron.:X*, 2024, 100527.
18 K. V. Serebrennikova, A. N. Berlina, D. V. Sotnikov, A. V. Zherdev and B. B. Dzantiev, *Biosensors*, 2021, **11**, 512.
19 M. Fan and A. G. Brolo, *ACS Nano*, 2025, **19**, 3969.
20 T. L. Valerio, R. Anastácio, S. S. da Silva, C. C. de Oliveira and M. Vidotti, *Anal. Methods*, 2024, **16**, 2164.
21 L. M. C. Ferreira, D. Lima, L. H. Marcolino-Junior, M. F. Bergamini, S. Kuss and F. C. Vicentini, *Bioelectrochemistry*, 2024, **157**, 108632.
22 D. W. Junior and L. T. Kubota, *Talanta*, 2024, 126467.
23 B. L. Garrote, F. C. B. Fernandes, E. M. Cilli and P. R. Bueno, *Biosens. Bioelectron.*, 2019, **127**, 215.
24 C. He, C. Lin, G. Mo, B. Xi, D. Huang, Y. Wan, F. Chen, Y. Liang, Q. Zuo and W. Xu, *Biosens. Bioelectron.*, 2022, **198**, 113857.
25 B. A. Taha, Y. Al Mashhadany, Q. Al-Jubouri, A. R. B. A. Rashid, Y. Luo, Z. Chen, S. Rustagi, V. Chaudhary and N. Arsad, *Sci. Total Environ.*, 2023, **880**, 163333.
26 J. R. Oliveira, C. M. R. Ruiz, R. R. G. Machado, J. Y. Magawa, I. P. Daher, A. H. Urbanski, G. J. H. Schmitz, H. A. Arcuri, M. A. Ferreira and G. L. Sasahara, *Front. Immunol.*, 2023, **13**, 1010105.
27 J. Turkevich, P. C. Stevenson and J. Hillier, *Discuss. Faraday Soc.*, 1951, **11**, 55.
28 J. N. B. D. Pelin, C. J. C. Edwards-Gayle, H. Martinho, B. B. Gerbelli, V. Castelletto, I. W. Hamley and W. A. Alves, *Dalton Trans.*, 2020, **49**, 16226.
29 N. S. Mandal, A. Chatterjee and P. Purkayastha, *J. Chem. Sci.*, 2021, **133**, 90.
30 I. Mukherjee, A. Chatterjee, M. Mukherjee and P. Purkayastha, *J. Phys. Chem. C*, 2024, **128**, 15194.
31 C. Zhang, X. Liang, T. You, N. Yang, Y. Gaoa and P. Yin, *Anal. Methods*, 2017, **9**, 2517.
32 A. Michota and J. Bukowska, *J. Raman Spectrosc.*, 2003, **34**, 21.
33 S. M. Ansar, X. Li, S. Zou and D. Zhang, *J. Phys. Chem. Lett.*, 2012, **3**, 560.
34 F. C. Marques, R. S. Alves, D. P. dos Santos and G. F. S. Andrade, *Phys. Chem. Chem. Phys.*, 2022, **24**, 27449.
35 O. Perzanowska, M. Majewski, M. Strenkowska, P. Głowala, M. Czarnocki-Cieciura, M. Mazur, J. Kowalska and J. Jemielity, *Sci. Rep.*, 2021, **11**, 15741.
36 V. S. D. Mesias, H. Zhu, X. Tang, X. Dai, Y. Guo, W. Liu and J. Huang, *Chem. Commun.*, 2021, **57**, 6979.
37 H. Jans, X. Liu, L. Austin, G. Maes and Q. Huo, *Anal. Chem.*, 2009, **81**(22), 9425.
38 C. B. P. Ligiero, T. S. Fernandes, D. L. D'Amato, F. V. Gaspar, P. S. Duarte, M. A. Strauch, J. G. Fonseca, L. G. R. Meirelles, P. B. da Silva, R. B. Azevedo, G. A. S. Martins, B. S. Archanjo, C. D. Buarque, G. Machado, A. M. Percebom and C. M. Ronconi, *Mater. Today Chem.*, 2022, **25**, 100924.
39 W. I. Goldburg, *Am. J. Phys.*, 1999, **67**, 1152.
40 K. Takahashi, H. Kato, T. Saito, S. Matsuyama and S. Kinugasa, *Part. Part. Syst. Charact.*, 2008, **25**, 31.
41 E. M. Materón, F. R. Gómez, M. B. Almeida, F. M. Shimizu, A. Wong, K. B. R. Teodoro, F. S. R. Silva, M. J. A. Lima, M. K. S. C. Angelim and M. E. Melendez, *ACS Appl. Mater. Interfaces*, 2022, **14**, 54527.
42 Z. Zhao, M. Ren, W. Zhang, Z. Chen, L. Zhang, X. Qu, J. Shi, W. Xia, X. Xu and Y. Yang, *LWT*, 2024, **212**, 117015.
43 Y. Xie, Q. Li, J. Chen, W. Yue, Z. Xia, M. Zeng, Y. He, Y. Zhao and X. Luo, *Sens. Actuators, B*, 2023, **394**, 134470.
44 S. W. Bishnoi, C. J. Rozell, C. S. Levin, M. K. Gheith, B. R. Johnson, D. H. Johnson and N. J. Halas, *Nano Lett.*, 2006, **6**(8), 1687–1692.
45 G. Plascencia-Villa, R. Mendoza-Cruz, L. Bazán-Díaz and M. José-Yacamán, *Nanopart. Biol. Med.: Methods Protoc.*, 2020, **2118**, 351.
46 X. H. You, Y. Liu, Y.-Y. Li, B. Zhao, Y. Yang, R. Weerasooriya and X. Chen, *Adv. Sens. Energy Mater.*, 2023, **2**, 100067.
47 P. S. Sfragano, G. Moro, F. Polo and I. Palchetti, *Biosensors*, 2021, **11**, 246.
48 C. Y. N. Nicoliche, A. M. Pascon, Í. R. S. Bezerra, A. C. H. de Castro, G. R. Martos, J. Bettini, W. A. Alves, M. Santhiago and R. S. Lima, *ACS Appl. Mater. Interfaces*, 2022, **14**, 2522.
49 I. Ielo, G. Rando, F. Giacobello, S. Sfameni, A. Castellano, M. Galletta, D. Drommi, G. Rosace and M. R. Plutino, *Molecules*, 2021, **26**, 5823.
50 A. R. P. Silva, M. S. Guimarães, J. Rabelo, L. H. Belén, C. J. Perecin, J. G. Farías, J. H. P. M. Santos and C. O. Rangel-Yagui, *J. Mater. Chem. B*, 2022, **10**, 3587.
51 Q. Li, X. Zhang, M. Chen, C. Luo, R. Yang, T. Bu, M. Dang, X. Huang, L. Song, P. Zhang, L. Liu and Y. Mao, *Food Chem.*, 2025, **463**, 141297.

52 W. Jeong, J. Bu, L. J. Kubiatowicz, S. S. Chen, Y. Kim and S. Hong, *Nano Convergence*, 2018, **5**, 38.
53 J. N. Y. Costa, G. J. C. Pimentel, J. A. Poker, L. Merces, W. J. Paschoalino, L. C. S. Vieira, A. C. H. Castro, W. A. Alves, L. B. Ayres, L. T. Kubota, M. Santhiago, C. D. Garcia, M. H. O. Piazzetta, A. L. Gobbi, F. M. Shimizu and R. S. Lima, *Adv. Healthcare Mater.*, 2024, **13**, 2303509.
54 C. Robinson, V. B. Juska and A. O'Riordan, *Environ. Res.*, 2023, **237**, 116877.
55 D. Vinod, S. Sadanandan and R. Rajamani, *Biosens. Bioelectron.:X*, 2024, **20**, 100531.
56 N. R. Faria, T. A. Mellan, C. Whittaker, I. M. Claro, D. S. Candido and S. Mishra, *et al.*, *Science*, 2021, **372**, 815.
57 R. Garg, Q. Liu, J. Van Kessel, A. Asavajaru, E.-M. Uhlemann, M. Joessel, G. Hamonic, Z. Khatooni, A. Kroeker, J. Lew, E. Scruten, P. Pennington, W. Deck, T. Prysliak, M. Nickol, F. Apel, T. Courant, A. A. Kelvin, A. Van Kessel, N. Collin, V. Gerdts, W. Köster, D. Falzarano, T. Racine and A. Banerjee, *Vaccine*, 2024, **42**, 125980.
58 D. Zhou, W. Dejnirattisai, P. Supasa, C. Liu, A. J. Mentzer, H. M. Ginn and Y. Zhao, *et al.*, *Cell*, 2021, **184**, 2348.
59 S. Balaban Hanoglu, D. Harmanci, S. Evran and S. Timur, *Bioelectrochemistry*, 2024, **160**, 108784.
60 B. A. Braz, M. Hospinal-Santiani, G. Martins, C. S. Pinto, A. J. G. Zarbin, B. C. B. Beirão, V. Thomaz-Soccol, M. F. Bergamini, L. H. Marcolino-Junior and C. R. Soccol, *Biosensors*, 2022, **12**, 885.
61 B. M. Hryniewicz, J. Volpe, L. Bach-Toledo, K. C. Kurpel, A. E. Deller, A. L. Soares, J. M. Nardin, L. F. Marchesi, F. F. Simas, C. C. Oliveira, L. Huergo, D. E. P. Souto and M. Vidotti, *Mater. Today Chem.*, 2022, **24**, 100817.
62 F. A. Nunez, A. C. H. Castro, I. P. Daher, E. Cunha-Neto, J. Kalil, S. B. Boscardin, A. J. C. Lanfredi, V. L. D. Oliveira and W. A. Alves, *Biosensors*, 2023, **13**, 371.
63 L. Liv and A. Bas, *Anal. Biochem.*, 2022, **657**, 114898.